This manuscript has been submitted for peer review in Contributions to Mineralogy and Petrology. Subsequent versions of this manuscript may have slightly different content. If accepted, the final version will be available via the Peer-reviewed DOI link on the EarthArxiv website. The authors welcome questions about this work.

Linking petrographic and geochemical indicators of melt reactions in pelitic migmatites and leucogranites

Oldman, C. J. [1], Warren, C. J. [1], Harris, N.B.W. [1], Kunz, B.E. [1], Spencer, C. J. [2], Argles, T.W. [1], Hammond, S.J. [1], Degli Alessandrini, G[.1.]

Affiliations:

1. School of Environment, Earth and Ecosystems, Faculty of Science, Technology, Engineering and Mathematics, The Open University, Walton Hall, Milton Keynes, MK6 6AA, United Kingdom
2. Department of Geological Sciences and Geological Engineering, Queen's University, Kingston, Ontario KL7 3N6, Canada

Corresponding author: BE Kunz, Barbara.kunz@open.ac.uk

ORCiDs:

CJ Warren: 0000-0003-2444-9737

NBW Harris:0000-0001-9387-2585

BE Kunz: 0000-0002-9492-1497

CJ Spencer: 0000-0001-5336-1596

TW Argles: 0000-0002-0484-4230

SJ Hammond: 0000-0002-7097-0075

This manuscript has been submitted for peer review in Contributions to Mineralogy and Petrology. Subsequent versions of this manuscript may have slightly different content. If accepted, the final version will be available via the Peer-reviewed DOI link on the EarthArxiv website. The authors welcome questions about this work.

Linking petrographic and geochemical indicators of melt reactions in pelitic migmatites and leucogranites

Oldman, C. J. [1], Warren, C. J. [1], Harris, N.B.W. [1], Kunz, B.E. [1], Spencer, C. J. [2], Argles, T.W. [1], Hammond, S.J. [1], Degli Alessandrini, G[1].

Affiliations:

1. School of Environment, Earth and Ecosystems, Faculty of Science, Technology, Engineering and Mathematics, The Open University, Walton Hall, Milton Keynes, MK6 6AA, United Kingdom
2. Department of Geological Sciences and Geological Engineering, Queen's University, Kingston, Ontario KL7 3N6, Canada

Corresponding author: BE Kunz, Barbara.kunz@open.ac.uk

Abstract

Anatexis in orogenic systems has wide-reaching implications for the structure, mechanical strength, and later exhumation of the middle crust during orogeny. Previous studies of melt reactions in metapelitic rocks have identified three major melt-producing reactions: fluid-present incongruent melting, fluid-absent muscovite dehydration melting, and fluid-absent biotite dehydration melting. Due to the composition of the reacting phases and the formation of peritectic phases, each of these reactions has implications for element mobilisation. Petrographic and geochemical signatures of melt reactant and product minerals allow different reactions to be identified and distinguished. Migmatites and leucogranites occur across the Himalaya in the Greater Himalayan Sequence (GHS). Using samples from the Alaknanda valley, near Badrinath in the Garhwal Himalaya, we identify petrographic and mineral compositional characteristics that suggest a progressive thermal sequence through the fluid-present, muscovite-dehydration, and later biotite-dehydration melting reaction fields, but a differential record. Samples from a single outcrop only preserve records for one reaction type, despite having experienced the same thermal history. Our observational and *in-situ* chemical data from feldspars, micas, and garnet reveal melt reaction systematics through peritectic crystallisation textures and large-ion lithophile element concentrations. Our results show that the mineral chemistry and petrographic observations are similar between (source) migmatites and (sink)

granites, and that together these datasets provide more powerful insight into migmatite and granite melting reaction history than bulk-rock data alone.

Key words: Partial melting, geochemistry, petrography, Himalaya, metamorphism

Introduction

Determining the melt reactions that have led to the creation of migmatites and granites in the continental crust is important for constraining trace element mobilisation (extraction, transport and concentration or dispersion). Many crustal granites are formed from the melting of meta-sedimentary rocks, particularly metapelites, which themselves formed during the metamorphism of mud-rich sediments (Patiño Douce et al 1990). Metapelitic rocks have well-characterised melt reactions (Figure 1), which may occur by (1) fluid-present melting involving muscovite, (2) fluid-absent (dehydration) melting of muscovite, and (3) fluid-absent (dehydration) melting of biotite, each with distinct peritectic (solid product) phases (Inger and Harris, 1992; 1993). Fluid-present melting produces only sillimanite or kyanite as a peritectic phase (reaction 1) (Patiño Douce and Harris, 1998), while muscovite dehydration melting produces both peritectic K-feldspar and an aluminosilicate (sillimanite or kyanite) phase (reaction 2) (Gardien et al., 1995; Patiño Douce and Harris, 1998; Pickering and Johnston, 1998). Biotite dehydration melting produces peritectic K-feldspar, garnet/cordierite, and rutile/ilmenite (reaction 3) (Breton and Thompson, 1988; Harris et al., 1995).

Fluid-present melting	Ms + Qz + Pl + H_2O = Als + Melt	(1)
Ms-dehydration melting	Ms + Qz + Pl = Kfs + Als + Melt	(2)
Bt-dehydration melting	Bt + Als + Qz + Pl = Kfs + Grt/Crd + Ilm/Rt + Melt	(3)

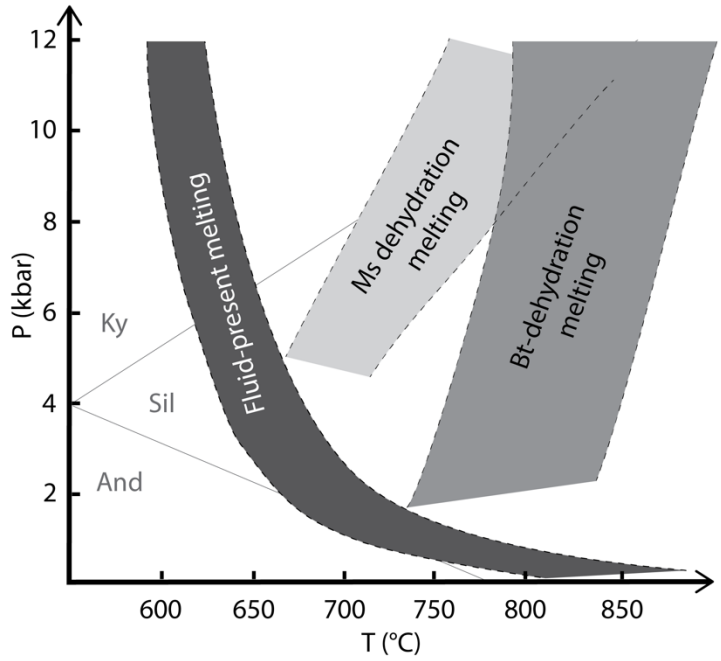

Figure 1: P-T diagram showing the the melt-forming reactions in metapelitic systems (after Weinberg & Haslova, 2015)

During melting, the composition of the reactant phases ultimately determines the available major and trace element budget, and during crystallisation, the composition of the product phases determines the element budget. The presence and amount of the peritectic products of melt reactions are of particular interest for constraining the mobility of trace elements in the crust as their formation varies with pressure and temperature, melt reaction, and they tend to remain in the source rock whereas the melt itself may be extracted (Vigneresse et al., 1996; Rosenberg and Handy, 2005; Brown, 2007). Elements that are hosted by the peritectic phases, e.g. Rb, Sr, Ba and Eu in the case of K-feldspar and Y and rare earth elements (REEs) in the case of garnet, are therefore fractionated between the restite and mobile melt.

Petrographic observations can be used to determine the (sequence of) melt reactions which may have occurred in a particular sample (e.g. Dyck et al 2020). For example, the presence of peritectic K-feldspar in a migmatite or leucogranite is indicative of muscovite dehydration melting, while peritectic garnet (or cordierite, depending on pressure and bulk composition) and K-feldspar together are indicative of biotite dehydration melting. Peritectic grains may be distinguished from melt-crystallised grains of the same phase by examining their textures. K-feldspar textures attributed to peritectic growth include the overgrowth and replacement of plagioclase, poikiloblastic grains, and porphyroblastic grains (Dyck et al., 2020). Garnet may be identified as peritectic by the presence

of very fine, randomly oriented inclusions in the cores of grains, primarily of apatite (Dorais and Campbell, 2022; Dorais and Spencer, 2014; Taylor and Stevens, 2010).

Petrographic observations may however not provide the full story. Textural overprinting may occur in systems that have experienced sequential melt-producing reactions, as peritectic sillimanite or kyanite formed through fluid-present melting may be indistinguishable from, or even overgrown by, later sillimanite/kyanite formed as a product of Ms-dehydration melting (Phillips et al., 2023). As such, potential differences in the geochemical signatures of melt reaction products due to varying reactant phases and proportions, tied to textural observations, may provide the best opportunity to interpret melt-reaction history. The large-ion-lithophile elements (LILEs) Rb, Sr, and Ba are of particular interest as melt reaction indicators, as these elements are predominantly hosted by the micas and feldspars involved in melt-producing reactions in metapelitic systems (Harris et al., 1995). Differences in the relative modal consumption of plagioclase, muscovite, and biotite in mica schists during melting have been suggested to result in bulk-rock leucosome or granite Rb/Sr of <2 for fluid-present melting and >5 for dehydration melting due to the varying Rb/Sr of each phase (Harris et al., 1993; Patiño Douce and Harris, 1998). Leucosomes or granites with relatively high bulk concentrations of Ba (a fluid-mobile element), are considered particularly indicative of fluid-present melting (Patiño Douce and Harris, 1998). Similarly, relatively high bulk concentrations of Ca, Zr, Hf, Th, and the light REEs and lower concentrations of Nb, Ta, and U suggest fluid-present melting Gao et al., 2017).

Most previous studies of migmatites and granites that have used chemical signatures to identify source melt reactions, including those referenced above, have based their interpretations on bulk rock chemical data (e.g., Inger and Harris 1993; Ji et al., 2023). Whilst these studies have provided important insights, the majority of migmatites are compositionally heterogeneous. Different portions of the rock may, due to lithological variability, record different metamorphic and melting reactions, therefore causing difficulties in determining the equilibrated bulk volume. Additionally, it is important to identify which minerals contribute or withhold which elements to/from the melt; this can only be achieved by *in-situ* measurements.

Here we link melt reactions and relative melt volumes interpreted from the petrographic observations to major and trace element compositions of feldspars, micas, and garnet to identify the chemical contributions of participating minerals that characterise the appropriate melt mechanism during anatexis. The geochemical data, alongside temperatures calculated using Ti-in-biotite

thermometry, provide further evidence for previous interpretations of, and insights into, anatectic mechanisms in the crust and the petrogenesis of crustal granites.

Methods

Detailed instrument and analytical conditions can be found in Online Resource 1.

Optical microscopy was carried out on polished thin sections with typical thicknesses of 35-40 µm to allow for in situ SEM and laser-ablation analysis of the observed textures. As such the photomicrographs under crossed-polarised light display higher-order interference colours than standard thin sections.

Whole-section Backscattered-Electron (BSE) and Energy Dispersive Spectroscopy (EDS) images and chemical maps were collected using an FEI Quanta 200 3D tungsten-filament SEM, fitted with an Oxford Instruments INCA EDS detector, at the Open University. The beam was set to a voltage of 20 keV and a current of ca. 1.2 nA. The resulting images were stitched together using the Oxford Instruments INCA software 'Montage' function. Garnet grains were picked from partially crushed samples at various size fractions to recover intact grains and were sorted into size fractions by diameter. Size fractions were mounted in resin blocks and polished to target the geographic cores of the grains.

The chemical compositions of major phases were collected by point and line analysis using a Zeiss Supra 55 VP field-emission SEM fitted with an Oxford Instruments X-Max 50 mm2 EDS detector at the Open University. The beam was set to a voltage of 20 kV and a current equivalent of 2.0 nA (60 µm aperture) with a 30 s acquisition time. Data were corrected for detector sensitivity loss using a natural almandine standard. Confidence in the precision of values is better than 0.3 oxide wt% (2σ).

Spot analysis concentrations of 54 major and trace elements were collected from micas, feldspars and garnet using a Photon Machines Analyte G2 193 nm excimer laser system equipped with a HelEX II laser ablation cell coupled with an Agilent 8800 Triple Quadrupole ICP-MS at the Open University. The ICP-MS was tuned using NIST SRM 612 glass prior to each analytical session to optimise sensitivity and reduce oxide production. Spot analyses were run using a fluence of 3.63 J/cm2, a repetition rate of 10 Hz, and a spot size of 50 µm, with each analysis collecting 30 seconds of background, 30 seconds of sample ablation, and 40 seconds of post-ablation washout. For feldspar

analyses in samples 04b, 07c, 09b, and 10, a pre-ablation laser pulse was performed to improve laser-sample coupling, followed by a 10-second pause before collecting background measurements. Spots were analysed in batches of twenty, bracketed by two analyses of NIST 612 and BCR-2G glass standards each. Data reduction was carried out using Iolite v3.71 (Paton et al., 2011), with baseline signal subtraction and time-resolved spectra checked for inclusion signals and ablation issues. Only stable signal sections were used for concentration calculations. NIST SRM 612 was used as the primary standard and BCR-2G as the secondary standard for most elements, though BCR-2G was used as the primary standard for Na, Mg, Al, P, K, Ca, Ti, Mn, and Fe, due to higher concentrations of these elements. Si was used for standardisation, with values taken from EDS measurements (either directly from the analysis site, or from averages of similar grains for each mineral phase where direct measurement was not possible). Indium concentrations were corrected for 115Sn isobaric interference. Accuracy and precision of BCR-2G analyses were in good agreement with published values (Jenner and O'Neill, 2012) and with relative standard deviations of 3-5% (Online Resource 2).

Ti-in-biotite temperatures were calculated using the Wu and Chen (2015) calibration with a pressure estimate of 1 GPa (peak calculated pressure conditions in the Badrinath Formation; Spencer et al., 2012a) and data from both the EDS and LA-ICP-MS datasets. Propagated uncertainty for the calibration is approximately ±65°C (Wu and Chen, 2015). Post-peak Fe-Mg diffusion between biotite and other ferromagnesian minerals, especially garnet, may increase the Mg concentration in biotite (Kohn and Spear, 2000). Higher Mg concentrations will have the effect of lowering the calculated Ti-in-biotite temperatures. This effect is strongest where garnet and biotite are in contact, therefore temperatures of biotite grains in contact with garnet were not calculated.

Sample petrography and modal abundances of major phases

Migmatite and leucogranite samples were collected from the Badrinath Formation of the Garhwal Himalaya in NW India, part of the upper sequence of the Great Himalayan Series, characterised by widespread anatexis and crustal leucogranites (Valdiya, 1979; Spencer et al., 2012a, Paul, 1998). Samples include pelitic/semi-pelitic migmatites and leucogranites that record various degrees of melting: from *in-situ,* disconnected leucosome lenses through interconnected leucosomes to more extensive granitic bodies. Samples were collected from localities displaying cross-cutting leucosomes and granites. Full sample descriptions, field photos, locality information and mineralogy are provided in Online Resource 3. Figure 2 shows the sampling localities.

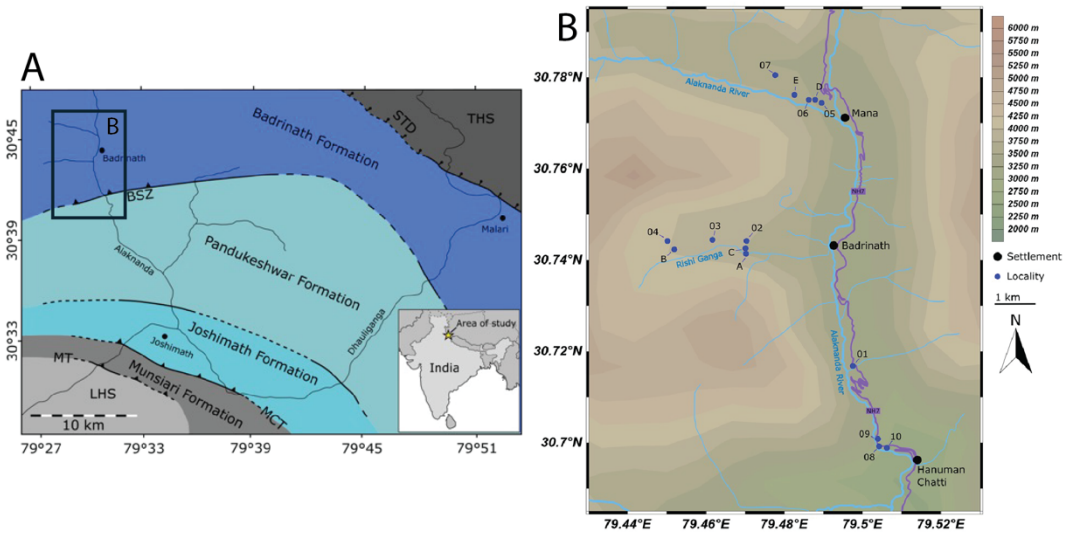

Figure 2: Map showing sample localities. (a) Simplified geological map of the GHS in the eastern Garhwal, showing the Alaknanda and Dhauliganga valleys, after Spencer et al., 2012a and references therein. Box shows location of (b). Inset shows the study area in relation to India. (b) Map of sampling localities along the Alaknanda and Rishi Ganga valleys, around Badrinath in the Garhwal Himalaya. Coordinates are in WGS84. Locality 11 is 15.5 km south-southeast of Hanuman Chatti, near Joshimath

Based on field (e.g. Sawyer, 2008) and thin-section scale textural differences (e.g. Erdmann et al., 2012; Dyck et al., 2020), migmatite and leucogranite samples were divided into three groups. Group 1 migmatites, samples 5b, 7c, 8, 9b, and 11, contain muscovite, biotite, quartz, garnet, sillimanite and plagioclase with minor K-feldspar. They are distinguished by the presence of discrete leucosomes, either as veins or irregular disconnected deformed domains (Figure 3a), and either lack, or have a low modal abundance (≤1%) of K-feldspar (Figure 3b). K-feldspar is present only in leucosomes and/or as fine, isolated grains in the phyllosilicate-rich schistose parts of the rock (melanosome). Plagioclase is present in both leucosomes and the schist (melanosome) (Figure 3b). Muscovite is a major component in the melanosome of samples 8, 9b and 11, with only rare grains in the leucosome. Muscovite in 5b and 7c occurs as relict grains associated with biotite or back reactions involving K-feldspar and sillimanite. Sillimanite varies from 0-5% modal abundance, with higher modal percentages associated with larger leucosome domains.

Group 2 migmatites, samples 2a, 4a, 4b, 7a, f02, and f13, contain muscovite, biotite, quartz, garnet, K-feldspar, sillimanite and plagioclase. In contrast with Group 1 samples, the leucosome domains have more diffuse boundaries (Figure 3c). The K feldspar is porphyroblastic in the mesosome and

phenocrystic in the leucosome, with grains >2 mm across (Figures 3c,d,e) with perthitic albite lamellae and inclusions of irregular quartz and embayed plagioclase. Samples 4b, 7a, f02, and f13 also contain lenticular clusters of K-feldspar grains in quartzofeldspathic domains. Plagioclase is either greatly reduced in abundance, or present as embayed inclusions within K-feldspar (Figure 3e) Sample 4a displays topotactic replacement of plagioclase by K-feldspar (Figure 3f). Sillimanite is present in clots associated with phyllosilicate domains (e.g. sample 7a) or as schlieren in leucosomes (e.g. sample 2a).

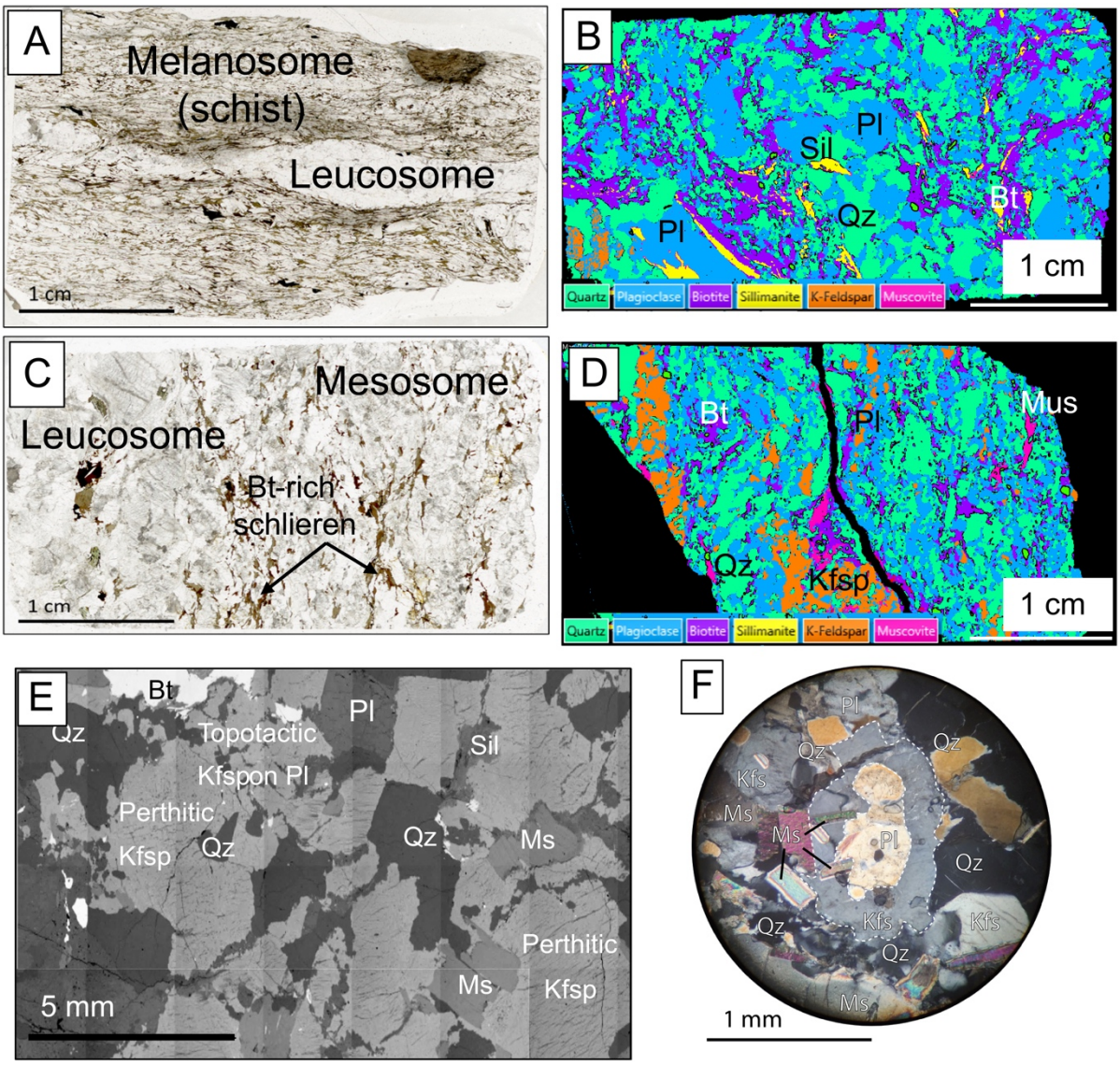

Figure 3: *Composite images showing Group 1 and 2 sample field relations and petrography. (a) Thin section photomicrograph of Group 1 migmatite 08. (b) False colour SEM image of diatexitic Group 1*

migmatite 07c. The leucosomes are the irregular areas of coarser Qz and Pl (centre and lower left). (c) Thin section photomicrograph of Group 2 migmatite 4b. (d) False colour SEM image of sample Group 2 migmatite 7a. The Kfsp defines the larger patches of leucosome, commonly also rimmed by Mus-Sil and Bt. (e) BSE image of sample 4a showing perthitic K-feldspar phenocrysts and K-feldspar overgrowing plagioclase. (f) Photomicrograph of sample 4a showing plagioclase with K-feldspar overgrowth/replacement in the mesosome

Leucogranite samples, 1d, 2b, 3, 7b, and f04, contain quartz, plagioclase and K-feldspar ± sillimanite, muscovite and rare garnet and biotite. They share distinctive microtextural features with the Group 2 migmatites: K-feldspar phenocrysts are perthitic, with inclusions of irregular quartz and embayed plagioclase (Figures in Online Resource 3), and are texturally similar to the porphyroblastic grains in many of the Group 2 migmatite samples (Figure 3e,f). Fibrolitic sillimanite is present in samples 1d, 7b and f04. Garnet in sample 1d (the only garnet-bearing leucogranite in this group) is elongate and contains a diverse population of <50 µm -sized inclusions in the cores (Figure 4a). Lobate quartz inclusions are randomly distributed throughout the grains. Based on the textural similarities, we interpret these leucogranites as having formed by the same melting reactions as the Group 2 migmatites and therefore also ascribe these to Group 2.

One leucogranite, sample 6, also contains quartz, plagioclase and K-feldspar ± muscovite and rare garnet. The garnet is distinctively different from the garnets in the migmatites and group 2 leucogranites. These grains are subhedral to euhedral with strongly developed optically-visible core-rim zoning. The cores are rich in randomly-oriented <10 µm inclusions of apatite, rutile, xenotime, and zircon, while the core-rim transition hosts crystallographically-oriented rutile needles up to 100 µm in length (Figure 4b,c) Pale pink garnet rims occasionally contain lobate quartz but are otherwise inclusion poor. This sample is separated from the others into a Group 3.

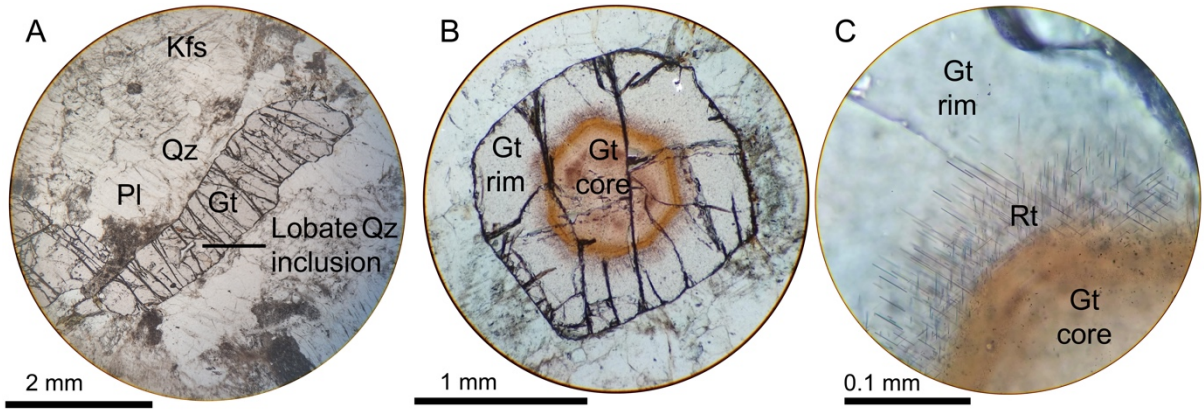

Figure 4: (a) Garnet in sample 1d showing lobate quartz inclusion (Group 2). (b, c) Garnet in sample 6 (Group 3), showing clear core rim distinction. (c) At the boundary of the core and rim fine needles or rutile can be observed

Table 1: Summary of sample groups

Group	Lithology	Sample number	Mineralogy (details in Online Resource 3)
1	Migmatite	5b, 7c, 8, 9b, 11	Qtz+PL+Ms+Bt+Gt+Sil±Ksp
2	Migmatite	2a, 4a, 4b, 7a, f02, f13	Qtz+Pl+Ksp+Bt±Sil±Ms±Gt
2	Leucogranite	1d, 2b, 3, 7b, and f04	Qtz+Pl+Ksp±Sil±Ms±Gt±Bt
3	Leucogranite	6	Qtz+Pl+Ksp±Ms±Gt

Linking petrography to melt reactions

The fluid-present melting reaction (1) predicts the formation of a peritectic aluminosilicate phase only. Migmatite Group 1 samples (Table 1) either lack K-feldspar completely or do not contain enough to be convincingly peritectic - the modal abundance of K-feldspar is too low relative to the volume of leucosome to satisfy the 4:5 stoichiometric ratio of peritectic K-feldspar to melt suggestive of muscovite dehydration melting (reaction 2) (Dyck et al., 2020). We therefore interpret these samples as recording fluid-present melting.

Migmatite Group 2 samples (Table 1) all contain porphyroblastic and poikiloblastioc K-feldspar or lenticular clusters of K-feldspar grains in quartzofeldspathic domains with little plagioclase and no

garnet. Following Dyck et al., 2020, we interpret the K-feldspar as having formed as a peritectic phase during muscovite dehydration (reaction 2).

The majority of the leucogranite samples also contain features suggestive of formation by muscovite dehydration melting, despite progressive melt amalgamation and migration. Leucogranite samples 01d, 02b, 03, 07b, and f04 feature two petrographic textures of K-feldspar: grains that are indicative of peritectic porphyroblasts, and smaller grains in the matrix that suggest direct crystallisation from the melt (Dyck et al., 2020). The former texture is interpreted as peritectic grains entrained into the melt from disaggregating source migmatites during melt amalgamation and migration (Brown, 2013). Samples 01d and 7b contain sillimanite schlieren with high aspect ratios, also suggesting a peritectic origin. Garnets in sample 01d contain lobate quartz inclusions (Figure 4a), suggesting crystallisation from the melt (Jung et al., 2022; Taylor and Stevens, 2010).

The garnet in sample 06, contains a high concentration of very fine, randomly oriented inclusions of apatite, rutile, xenotime and zircon in their cores. These inclusions are suggestive of a peritectic origin for the garnet cores (Dorais and Campbell, 2022; Dorais and Spencer, 2014; Taylor and Stevens, 2010). The porphyroblastic K-feldspar grains in this sample are petrographically identical to those in Group 2 samples, also suggestive of a peritectic origin. Together, the K-feldspar and garnet suggest that leucogranite 06 formed through the biotite dehydration reaction (reaction 3) (Breton and Thompson, 1988; Harris et al., 1995). The garnet rims occasionally contain lobate quartz inclusions similar to those in the garnet in sample 01d, suggesting that the garnet rims formed during magmatic crystallisation.

In summary, the petrographic observations suggest that Group 1 migmatites (05b, 07c, 08, 09b, and 11) preserve a textural record of fluid-present melting. Group 2 migmatites (02a, 04a, 04b, 07a, f02, and f13) and all but one leucogranite sample (01d, 02b, 03, 07b, and f04) preserve a textural record of muscovite dehydration melting. Group 3 leucogranite 06 preserves a textural record of biotite dehydration melting.

Ti in biotite concentrations and temperatures

All biotite contains Al/Si and Fe/Mg typical of siderophyllite-annite compositions (Deer et al., 2013) and most contain 0.12 – 0.24 Ti a.p.f.u. (Group 2 leucogranite sample 03 has elevated Ti concentrations of 0.26 Ti a.p.f.u). No biotite was present in Group 3 sample 06. The EDS and LA-ICP-MS Ti concentration datasets yield a maximum temperature difference of 20°C (Table 2). Figure 5

therefore shows the LA-ICP-MS data only for samples for which no EDS data were collected. The data in Table 2 and presented on Figure 5 contain only the data for which Ti concentrations and X_{Mg} fall within the Wu and Chen, 2015 calibration range. The full Ti in Bt (TiB) dataset is presented in Online Resource 4.

Table 2: Calculated Ti in Bt temperatures, presented to the nearest 1°C for 1 GPa pressure. L=leucogranite, M=migmatite, n= number of datapoints lying within the Wu and Chen, 2015, calibration range.

Sample	Group	Lithology	Dataset	n					
					Max	Min	Mean	Median	Stdev
07c	1	M	EDS	42	690	633	670	672	13
			LA-ICP-MS	8	696	650	678	683	17
08	1	M	EDS	18	715	663	690	669	16
			LA-ICP-MS	-	-	-	-	-	-
09b	1	M	EDS	6	766	674	729	749	30
			LA-ICP-MS	6	804	707	756	755	29
02a	2	M	EDS	10	791	756	775	778	12
			LA-ICP-MS	-	-	-	-	-	-
04a	2	M	EDS	15	787	738	760	758	14
			LA-ICP-MS	-	-	-	-	-	-
04b	2	M	EDS	7	771	742	760	761	10
			LA-ICP-MS	5	809	764	779	771	16
07a	2	M	EDS	9	784	760	776	775	7
			LA-ICP-MS	4	790	759	777	779	12
f02	2	M	EDS	-	-	-	-	-	-
			LA-ICP-MS	5	825	714	784	811	45
01d	2	L	EDS	18	776	675	726	720	30
			LA-ICP-MS	4	742	696	717	715	18
03	2	L	EDS	11	745	720	730	731	7
			LA-ICP-MS	12	751	675	707	710	21

07b	2	L	EDS	11	807	790	797	797	6
			LA-ICP-MS	5	811	781	798	803	12
f04	2	L	EDS	-	-	-	-	-	-
			LA-ICP-MS	9	833	748	799	803	23

Calculated TiB temperatures across all ss range from 633–833°C, with a maximum variation within any given sample of 110°C (Table 2, Figure 5). Group 1 migmatites 07c and 08 yield median temperatures <700°C, whereas Group 2 migmatites 02a, 04a, 04b, and 07a yield median values of 750–780°C. Group 1 migmatite sample 09b yielded an intermediate temperature, with median values of ~750°C. Group 2 migmatite sample f02 yielded a notably higher median value of 810°C and the largest intrasample variation. Group 2 leucogranite samples 01d and 03 yield the lowest median temperatures of 710-730°C, while leucogranite samples 07b and f04 yield higher median temperatures of ~800°C (Figure 5).

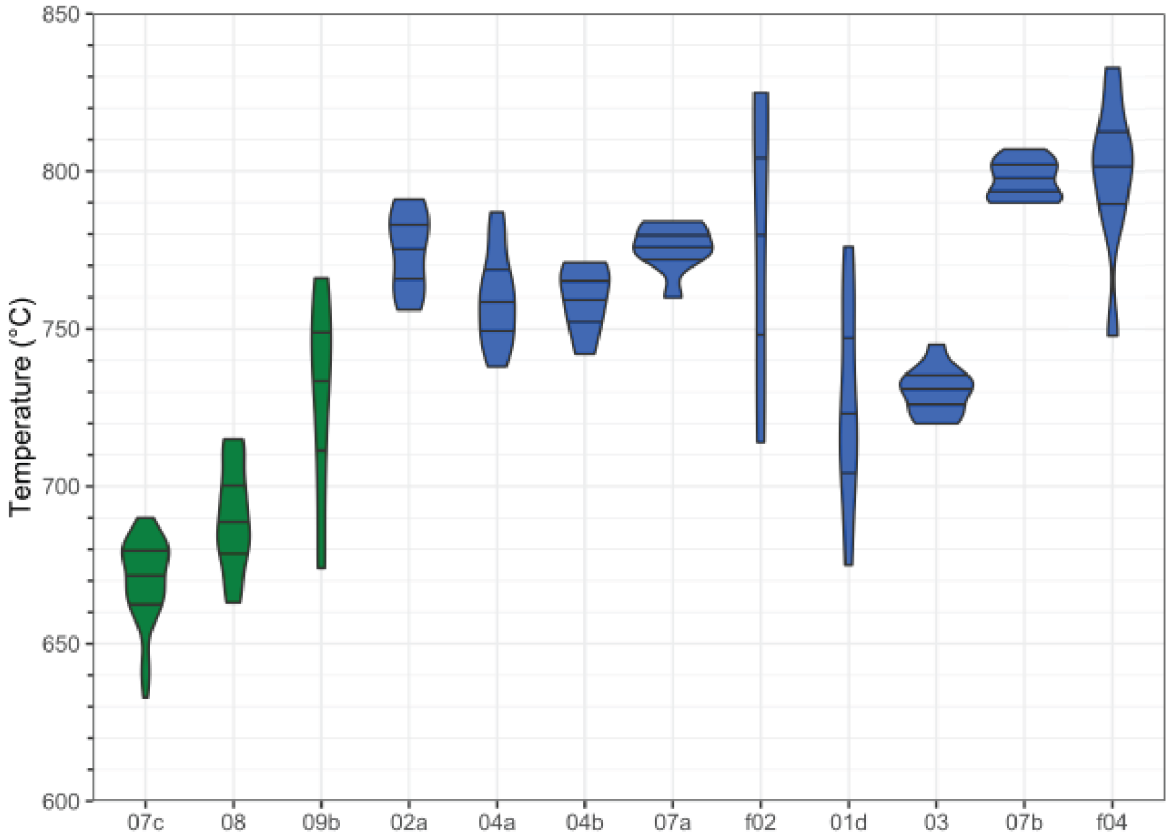

Figure 5: Violin plots of calculated Ti in Bt temperatures for Group 1 (green) and Group 2 (blue) migmatite (02a, 04a, 04b, 07a, f02) and leucogranite (01d, 03, 07b, f04) samples. All data are from EDS apart from samples f02 and f04, for which the LA-ICP-MS data are plotted. The dashes mark the upper quartile, median and lower quartile respectively. The width of the "violins" corresponds to the number of datapoints yielding that value of temperature

Thermal evolution

Titanium in biotite thermometry calculations for the migmatites and leucogranites yield temperatures that correlate with petrographic observations of fluid-present and muscovite dehydration melting. Group 1 migmatites typically record temperatures <700°C and Group 2 typically record temperatures >750°C. The increase in temperature is consistent with that expected for the relative temperatures of fluid-present and muscovite dehydration reactions (Figure 1, e.g. Clemens, 1987; Le Breton and Thompson, 1988). Two observations require discussion – the differing temperature records of two samples from the same outcrop and differing temperature records of different Group 2 leucogranites.

Group 1 migmatite sample 7c was collected from within roughly a meter of Group 2 migmatite sample 7a (Figure 6), and a similar overall thermal evolution would therefore be hypothesised. However, sample 7c records a significantly lower temperature (average 680°C vs average 780°C). The recorded temperatures are consistent with the expected temperatures for the melting reactions the samples record (fluid-present in sample 7c and muscovite dehydration in sample 7a). We suggest that after cessation of the fluid-present melting which reacted out most of the muscovite, biotite in sample 7c failed to re-equilibrate at higher temperatures – maybe due to lower a_{TiO_2} compared to the Group 2 samples.

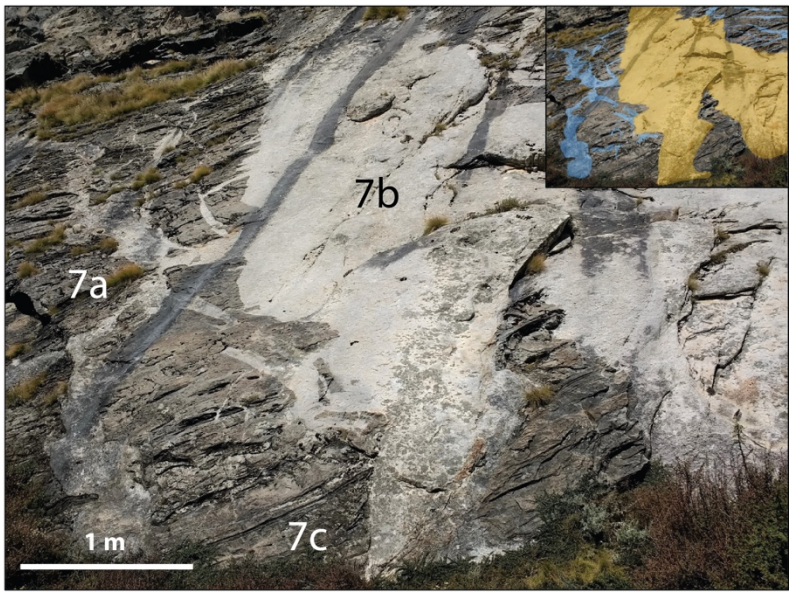

Figure 6: Field photograph of cross-cutting relationships in Locality 7. Inset shows interpretation of cross-cutting leucosome relationships with the yellow leucogranite (sample 7b) cross-cutting the blue leucosome (not sampled). Migmatite samples 7a and 7c showed different leucosome expressions and proportions.

The dependence of Ti concentrations in biotite on temperature has long been recognised (Henry and Guidotti 2002) but no single Ti exchange reaction (exchanging Fe, Mg or Al for Ti) accounts for the total temperature effect. Calibrations also assume Ti saturation (in effect buffered by either rutile or ilmenite; Wu and Chen 2015); Ti contents of micas often approximate expected compositions in equilibrium with rutile, even when rutile is not present, suggesting that metapelites are generally near rutile saturation (Chambers and Kohn, 2012). As such, the reliability of Ti in biotite concentrations to relate to temperatures of equilibration depends on the activity of TiO_2 (a_{TiO_2}) within a sample for given P-T conditions.

Previous studies have shown $a_{TiO_2} \approx 1$ in metapelitic bulk compositions at 650-700°C and 0.9-1.0 GPa (Ashley and Law, 2015). Their modelling shows that the a_{TiO_2} drops rapidly at the rutile-out boundary (temperatures >700°C for a pressure of 0.9-1.0 GPa; Meinhold, 2010). At these, and higher, temperatures, therefore, the relationship between temperature and Ti in biotite changes, and any temperatures calculated using the TiB calibration should consider this reduction in activity. The a_{TiO_2} may also be reduced by the presence of melt, as modelling from granitoid and rhyolitic melt suggests a_{TiO_2} values of <0.5 relative to rutile saturation (Borisov and Aranovich, 2020; Schiller and Finger, 2019). As such, the Ti-in-biotite temperature may record the point at which the presence of interstitial melt reduces the effective transfer of Ti^{2+} and Mg^{2+} ions between biotite and the matrix. Later increases in temperature of such previously-melted rocks may not be recorded.

The second thermal record disparity revolves around Group 2 leucogranite samples 01d, 03, 07b, and f04. These samples show petrographic textures, and record chemical indicators, of muscovite-dehydration melting, however also record two distinct temperatures, with 01d and 03 recording average temperatures of around 720-730°C, and 07b and f04 recording temperatures of around 800°C. The difference of 70-80°C, although only just outside the 65°C uncertainty of the calibration, appears to be linked to structural height through the GHS. Samples 01 and 03 were collected south of Bradrinath (Figure 2), whereas 07b and f04 were collected from stratigraphically higher positions. Spencer et al., 2012a also documents higher T with structural height. This could be accounted for by structurally higher samples being exhumed from deeper levels of the GHS, though precise pressure and timing constraints would be required to prove this.

Group 3 sample 06 contains garnets that themselves contain crystallographically-oriented rutile needles surrounding the core. This feature is commonly associated with garnet crystallisation temperatures of >800°C (Hwang et al., 2007; Proyer et al., 2013; Axler and Ague, 2015). At these temperatures Ti is more soluble in garnet; later cooling drives exsolution and crystallisation of rutile needles along the garnet (111) plane (Hwang et al., 2016). The high initial Ti concentrations in garnet in sample 06 therefore suggest higher temperature conditions than the other samples reported here.

Geochemistry Results

Full major element compositions and standard data are presented in Online Resource 5. Full LA-ICP-MS trace element compositions and standard data are presented in Online Resource 6.

We analysed 54 elements in the major minerals. Here we concentrate on reporting and interpreting Rb/Sr and Ba concentrations in K-feldspar, plagioclase, muscovite and biotite, in addition to Eu concentrations in the feldspars and Sn concentrations in the micas. These elements were shown in previous bulk rock studies to provide good indicators of melt reaction, as they are differentially hosted in either the reactant mica or the product feldspar: muscovite preferentially hosts Rb, Sr and Ba (until it starts to melt, at which point Ba partitions into the melt); biotite preferentially hosts Rb and Sn; plagioclase preferentially hosts Sr; and K-feldspar preferentially hosts Ba (Patiño Douce and Harris 1998, Harris et al., 1993, Gao et al., 2017).

K-feldspar

Major element compositions in K-feldspar do not relate to the petrographic groups, with all K-feldspar compositions ranging from $Or_{0.85-0.95}$. The trace element concentrations cluster into the sample groups determined by petrography. K-feldspar in all lithologies contains 170-1050 ppm Rb, 16-350 ppm Sr, 15-7200 ppm Ba, 0.1-2 ppm Eu, and Rb/Sr between 1-35. Group 1 samples yield the lowest Rb/Sr and highest Ba and Eu concentrations. Group 3 sample yield the highest Rb/Sr and lowest Ba and Eu concentrations (Figure 7), with Group 2 samples yielding more of a spread in Ba and Eu concentrations and Rb/Sr.

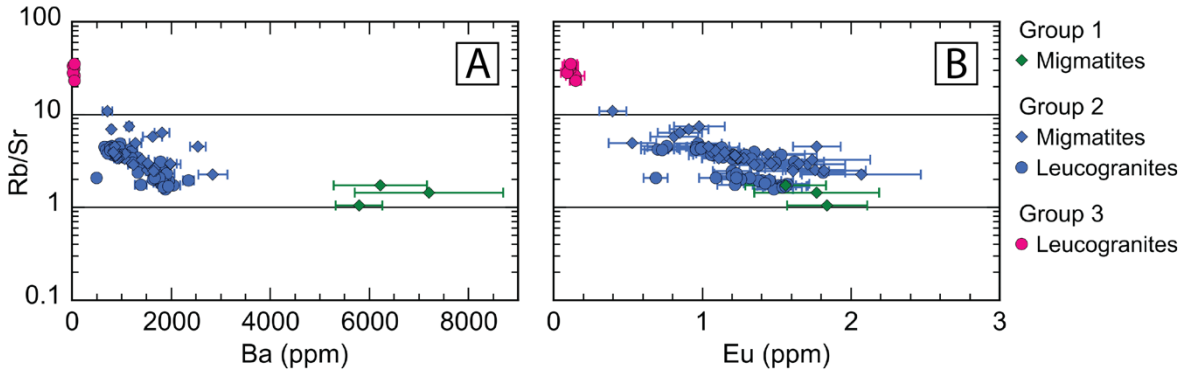

Figure 7: Rb/Sr in K-feldspar plotted against (a) Ba and (b) Eu

Plagioclase

Plagioclase shows more major and trace element compositional variation than K-feldspar across both the migmatites and leucogranites, with no link between major element composition and petrographic group. Plagioclase in Group 1 and 2 migmatite samples 04a, 04b, 07a, 07c, 08, 09b and f02 and leucogranite samples 01d, 07b, and f04 cluster between $An_{0.3-0.4}$; plagioclase in Group 2 migmatites 02a and f13, and leucogranite samples 02b (Group 2) and 06 (Group 3) is more albitic, clustering between $An_{0.2-0.3}$. Plagioclase in Group 2 leucogranite sample 03 is the most anorthitic, at ~$An_{0.45}$. Plagioclase in all other leucogranite samples is zoned, with oligoclase ($An_{0.1-0.3}$) to andesine ($An_{0.3-0.5}$) cores and more albitic ($An_{0-0.1}$) rims.

Plagioclase in all lithologies contains 0.1-360 ppm Rb, X-540 ppm Sr, 0.6-1690 ppm Ba, 0.04-3 ppm Eu, and Rb/Sr from 4 $x10^{-4}$ – 1.4. Group 1 migmatites contain the highest, and Group 3 leucogranite the lowest, Ba and Eu concentrations (Figure 8), whereas Rb/Sr values show a similar spread across all three sample groups.

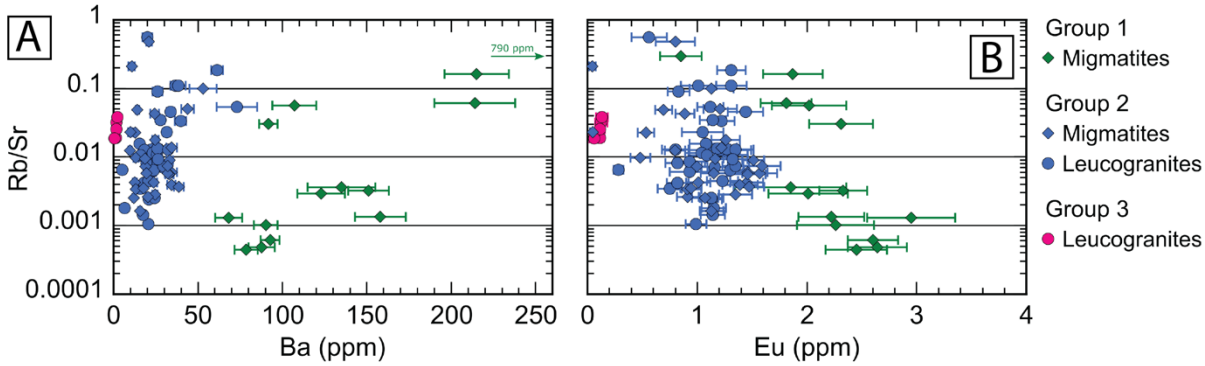

Figure 8: Rb/Sr in plagioclase plotted against (a) Ba and (b) Eu

Muscovite

Muscovite major element compositions in all samples lie within the typical range for muscovite in pelites (Forshaw and Pattison, 2021). Muscovite in all lithologies contains 270-1320 ppm Rb, 0.8-50 ppm Sr, 9-8640 ppm Ba, 13-720 ppm Sn, and Rb/Sr from 6-842. Ba and Sn showed the strongest correlations with Rb/Sr and concentrations of these elements differ between the sample groups (Figure 9). Muscovite in migmatite Group 1 samples contain the highest Ba concentrations and lowest Sn concentrations. Muscovite in Group 3 leucogranite 6 records the highest Rb/Sr, lowest Ba and generally high Sn. Group 2 migmatite sample f13 also yielded two muscovite analyses that are particularly Sn-rich at 190 and 723 ppm.

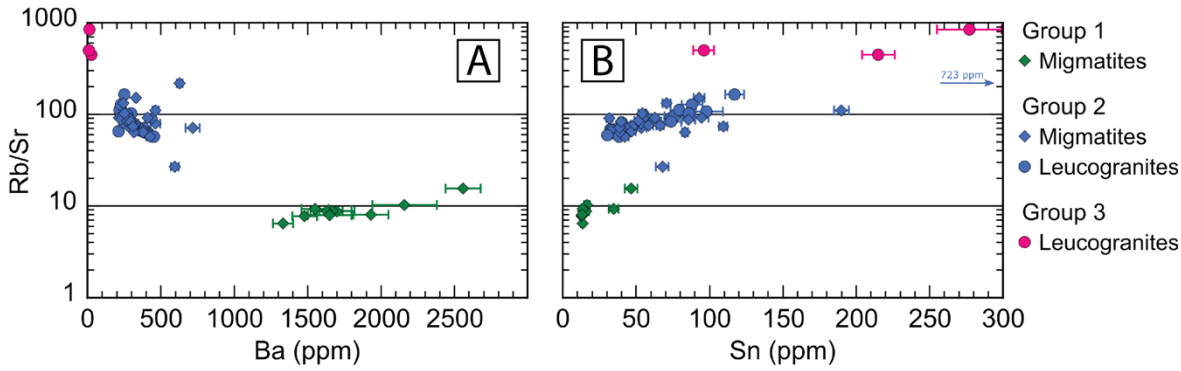

Figure 9: Rb/Sr in muscovite plotted against (a) Ba and (b) Sn

Biotite

No biotite was observed in Group 3 sample 6. Biotite in all other samples is of siderophyllite-annite composition (Deer et al., 2013) and contains 0.3-2560 ppm Rb, 0.2-74 ppm Sr, 0.1-1240 ppm Ba, 0.6-406 ppm Sn, and Rb/Sr from 78-5740 (Figure 10). Biotite in Group 1 migmatites contains higher Ba concentrations and lower Rb/Sr values than those in Group 2 migmatite and leucogranites. Biotites in Group 2 migmatite f13 contain significantly higher Sn concentrations than other samples (172-406 ppm).

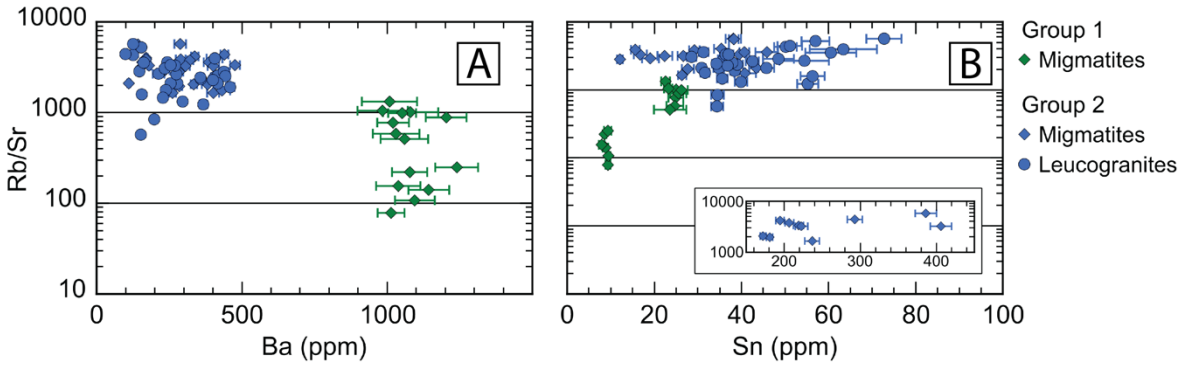

Figure 10: Rb/Sr in biotite plotted against (a) Ba and (b) Sn

Garnet

Garnets in the Group 1 migmatites were not analysed. Garnets in the Group 2 migmatites and leucogranites are Fe- and Mg-rich, and Ca- and Mn-poor. Migmatitic garnets record flat major element profiles except at the very outer rims (Figure 11a). Leucogranite garnets record flat Fe, Mg

and Ca profiles but commonly show cores enriched in Mn (Figure 11b). In contrast, garnets in Group 3 leucogranite sample 6 are Mn-rich, and Mg-poor and record more zoning in major elements, with core, mantle and rim zones most clearly demarked by Mn concentrations (Figure 11c). Garnets in sample 06 are also zoned in minor and trace elements (Online Resource 7). The core was too inclusion-rich to collect trace element concentration data that could definitively be linked to being hosted in garnet.

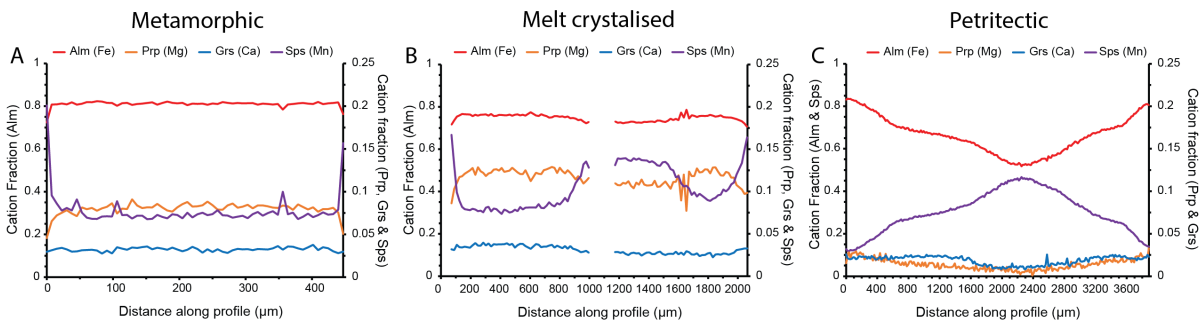

Figure 11: Garnet composition data. (a) Major element profile of garnet in Group 2 migmatite f02. (b) Major element profile of garnet in Group 2 leucogranite 1d. (c) Major element profile of garnet in Group 3 leucogranite 6

Chemical signatures of melting reactions

The in-situ mineral chemistry dataset complements and supplements the petrographic observations that are suggestive of the melting reaction(s) experienced by each sample. As the main phases involved in melting reactions in these rocks (micas, feldspars and garnet) may have different petrogenetic origins (metamorphic, peritectic, melt-crystallised or a combination, c.f. Phillips et al., 2022), we interrogated the chemical signature of each melting reaction with respect to the petrogenetic origin of the phases to determine any trends.

Petrogenesis vs chemical signature of fluid-present melting (Group 1 samples)

The Group 1 samples are migmatites that present sharp boundaries between the melanosome and leucosome, and in which the leucosomes are discontinuous and lenticular. These rocks are therefore interpreted as a migmatite where the melt portion formed in-situ and did not mobilise (far). The micas (predominantly biotite), garnet and plagioclase in the melanosome therefore formed during

sub-solidus metamorphic reactions, whereas the K-feldspar and plagioclase in the leucosome most likely formed from the crystallisation of melt.

All analysed minerals in the Group 1 samples show similar trends of lower Rb/Sr and higher Ba, with K-feldspar showing the clearest trends. The feldspars furthermore show the highest Eu concentrations of all the groups, and the micas show the highest Sn concentrations. These signatures mirror those of the bulk rock granites that were interpreted as formed through fluid-present melting reactions (Inger and Harris, 1993; Harris et al., 1993; Gao et al., 2017, Ji et al., 2023). This shows that there is a clear chemical link between the melt source (our rocks) and the melt sink (the granites analysed in the previous studies).

The chemical signatures in the Group 1 minerals indicate a low ratio of muscovite to plagioclase during melting, and consequently more release of Ba, Sr and Eu into the melt from plagioclase than Rb and Sn from muscovite. The low ratio of muscovite to plagioclase is consistent with balanced fluid-present muscovite melting reactions (Harris et al., 1995; Patiño Douce et al., 1998).

The diagnostic *petrographic* feature of fluid-present melting is the lack of peritectic K-feldspar and a modal abundance of melt-crystallised K-feldspar per volume of leucosome lower than 4:5 (Dyck et al., 2020). The diagnostic *chemical signature* of fluid-present melting in all analysed minerals is their relatively high Ba concentration compared with the other groups. This is also true for biotite, which in these samples was not involved in the melting reaction. Our interpretation is that biotite readily equilibrates with its environment, potentially incorporating Ba from fluids released during melt crystallisation.

Petrogenesis vs chemical signature of muscovite dehydration melting (Group 2 samples)

The Group 2 migmatite samples show more evidence for progressive melting than the Group 1 samples. They have diffuse boundaries between the mesosome and leucosome, and in the more diatexitic samples, contain diffuse melanosome patches that are likely remnants of the former schist. The micas and plagioclase, associated mainly with the mesosome and melanosome portions, have petrographic features that are consistent with their formation through sub-solidus metamorphic reactions. The garnets in the migmatites show chemical similarity to Group 1 garnets and are therefore also likely to be of metamorphic origin. The K-feldspar, associated with both the mesosome and leucosome, has petrographic features suggestive of both peritectic (in the mesosome) and melt-crystallised (in the leucosome) formation. In the mesosome, porphyroblastic K-

feldspar contains perthitic albite lamellae and inclusions of irregular quartz and embayed plagioclase. In some locations it replaces plagioclase topotactically. In the leucosome, K-feldspar commonly exhibits lenticular clusters. Compared with Group 2 sample, plagioclase is greatly reduced in abundance, and present as embayed inclusions within K-feldspar.

The Group 2 leucogranite samples show similar petrographic features to the minerals in the leucosomes of the migmatites. These include perthitic K-feldspar phenocrysts with inclusions of irregular quartz and embayed plagioclase that are texturally similar to the porphyroblastic grains in many of the Group 2 migmatite samples. The garnets, however, contain cores richer in spessartine, suggesting a magmatic origin (Müller et al., 2012).

Compared to the same minerals in Group 1 samples, the (reactant) muscovite, and biotite record higher Rb/Sr, higher Sn and lower Ba concentrations. The (product) K-feldspar has higher Rb/Sr, and both K-feldspar and plagioclase have lower Ba and Eu concentrations. These signatures mirror those of the bulk rock granites that were interpreted as formed through muscovite dehydration reactions (Inger and Harris, 1993; Harris et al., 1993; Gao et al., 2017, Ji et al., 2023). The overlap between the source migmatites and eventual granites that show the same petrographic signatures suggests little additional chemical differentiation during melt mobilisation. Additionally, the chemical similarity between reactant and product phases in the migmatites suggests chemical equilibration over the timescales of melting and cooling.

The chemical signatures of the Group 2 minerals indicate a higher ratio of muscovite to plagioclase consumption during melting than in the Group 1 samples: the reaction products (peritectic K-feldspar and melt) are more enriched in trace elements derived from muscovite (Rb and Sn), than those derived from plagioclase and fluid (Sr, Eu, and Ba, e.g. Harris et al., 1993, 1995; Gao et al., 2017). These chemical signatures are indicative of muscovite dehydration reactions.

Group 2 samples show a significant compositional spread in trace element concentrations both within and between samples, and between migmatites and granites. This spread may indicate variability in protolith bulk composition, a mixture of petrogenetic mineral origins (e.g. metamorphic, peritectic or crystallised from melt) or growth zoning formed during the progression of the melting reaction (e.g. peritectic cores and melt-crystallised rims, or multiple melt-crystallised zones that capture chemical evolution of the melt). In particular, our dataset shows no clear links between K-feldspar evolution in a single sample and chemical trend, nor clear differentiation between the chemical composition of K-feldspar in the source migmatites (potentially more

weighted towards peritectic formation) and the composition in the leucogranites (potentially more weighted towards magmatic formation). The petrographic features such as topotactic replacement of plagioclase by K-feldspar, clustered and annealed K-feldspar poikiloblasts with common inclusions of quartz and biotite, and K-feldspar porphyroblasts with poikiloblastic cores suggest a progressive record of melting (Erdmann et al., 2012; Dyck et al., 2020).

The diagnostic *petrographic* features of muscovite dehydration melting, therefore, are perthitic porphyroblasts of K-feldspar, clustering and annealing of K-feldspar poikiloblasts, K-feldspar porphyroblasts with poikiloblastic cores, and topotactic replacement of plagioclase by K-feldspar (Erdmann et al., 2012; Dyck et al., 2020). The diagnostic *chemical signature* of muscovite dehydration melting is the spread in Rb/Sr, Ba and Sn concentrations compared with other groups and the overall trend towards higher Rb/Sr and lower Ba in K-feldspar, as also shown in granite bulk rock data (Inger and Harris, 1993; Harris et al., 1993; Gao et al., 2017, Ji et al., 2023).

Petrogenesis vs chemical signature of biotite dehydration melting (Group 3 samples)

In this study, only a single granite sample was identified as being significantly different enough petrographically from the Group 2 leucogranites (due to the presence of peritectic garnet) to warrant its classification as a separate group. No migmatites were identified as containing peritectic garnet – the prediction is that these should exist somewhere as the protolith of this granite, but may well not yet be exposed. In the Group 3 leucogranite, the garnet was identified as peritectic due to its inclusion-rich core. Some of the K-feldspar might also be of peritectic origin, but the majority of the minerals show petrographic features that are more consistent with crystallisation from melt. No biotite was found in this sample.

Compared to the same minerals in Group 1 and 2 samples, all analysed minerals had higher Rb/Sr and very low Ba concentrations. Eu concentrations in feldspars were also very low but Sn in muscovite was generally high but variable. These signatures mirror those of the bulk rock granites that were interpreted as formed through biotite dehydration reactions (Inger and Harris, 1993; Harris et al., 1993; Gao et al., 2017, Ji et al., 2023). Biotite is a major reservoir of Rb and Sn in metapelites, and is also depleted in Sr relative to muscovite and plagioclase (Harris et al., 1995; Kunz et al., 2022). The high Rb/Sr in the K-feldspar and the high Sn in the magmatic muscovite, as well as the presence of peritectic garnet, therefore strongly suggest that biotite dehydration reactions were predominantly responsible for the formation of leucogranite sample 06.

The garnets in sample 06 show evidence of a complex history. The Mn- and inclusion-rich cores suggest formation via a peritectic reaction. The mantles containing crystallographically-oriented rutile needles and rims containing lobate quartz inclusions, suggest one and potentially two stages of later crystallisation from a melt (Jung et al., 2022, Taylor and Stevens, 2010).

Due to the inclusion-rich nature of the cores, the trace element composition of the host garnet itself was irretrievable. Similar HREE zoning patterns to those described from sample 06 garnet mantle and rim are described in granite-hosted peritectic garnets from the Mkhondo Valley Metamorphic Suite, Eswatini. These were interpreted as showing that the growth rate of the peritectic garnet was faster than the rate of HREE-rich accessory phase dissolution in the melt, and therefore demonstrated chemical disequilibrium between the garnet and the melt (Taylor and Stevens, 2010).

Summary

In general, we note the following overarching observations/interpretations:

1. Despite the fact that the main phases involved in melting reactions in these rocks (micas, feldspars and garnet) may have different petrogenetic origins (metamorphic, peritectic, melt-crystallised or a combination, c.f. Phillips et al., 2022), our dataset shows no chemical trends on the grain or thin section scale. This may be due to rapid chemical equilibration at high temperatures or due to the ablation volume of our analytical spots being bigger than potential trace element zoning. We did not design our sampling strategy with chemical zoning in mind, but this is something that may be of interest for future work.
2. The overall trends in our migmatite and leucogranite data are the same as the overall trends in the bulk rock data because the trends are dominated by the minerals that we have investigated: muscovite releases Rb, Sr and Ba into the melt; biotite releases Rb and Sn; plagioclase releases Sr; and K-feldspar releases Ba (Patiño Douce and Harris 1998, Harris et al., 1993, Gao et al., 2017).
3. K-feldspar chemistry provides the clearest indicator of reaction – it shows the clearest trends and is present in all the samples even though its petrogenesis varies.

Discussion

Our new in-situ chemical dataset of reactant (metamorphic) and product (peritectic and magmatic) minerals in Himalayan migmatites and leucogranites complements and supplements the petrographic observations that suggest their melting history. Furthermore, the *combination* of chemistry and petrography still allows the melting reaction to be identified even in cases where the melt has left the source region (leucogranites), or where the progression of melting has (partially) overprinted petrographic evidence (e.g. diatexites).

Our geochemical dataset of melting reaction mineral reactants and products in migmatites and leucogranites shows clear trend similarities with published leucogranite bulk rock data (Inger and Harris 1993; Gao et al., 2017, Ji et al., 2023). K-feldspar, whether in migmatite leucosomes or in leucogranites, records the same geochemical vector directions for the three melting reactions as originally recorded in the bulk rock leucogranite data. Petrographic and chemical evidence for biotite dehydration melting is rare in the Himalaya as a whole, so it remains to be seen whether these trends appear in migmatites formed by biotite-dehydration reactions in other regions.

Metapelites will only experience fluid-present melting if there is sufficient availability of fluid at the right PT conditions. In our samples, there is no textural or chemical evidence that Group 1 migmatites experienced muscovite dehydration melting after fluid-present melting despite regional temperatures that facilitated muscovite dehydration in the surrounding area – this is likely because all the muscovite reacted. Equally, there is no textural or chemical evidence that Group 2 migmatites experienced fluid-present melting before muscovite dehydration melting. This suggests that fluid infiltration was localised, and once melting was complete, there was little additional chemical re-equilibration. Evidence for this is suggested by the lower Ti-in-biotite temperatures recorded in these samples, despite the increasing ambient temperatures (as evidenced by the temperatures recorded by sample 7a (Group 2 migmatite, 780°C), collected adjacent to sample 7c (Group 1 migmatite, 680°C).

There is also no petrographic or chemical evidence in the single biotite dehydration sample for any evidence of mixing with melt produced by muscovite dehydration melting. However, the high temperatures experienced by this sample may have facilitated efficient chemical equilibration between and within the different constituent minerals, thus removing evidence for any earlier thermal history.

The Garwhal Himalaya do not appear to expose leucogranite bodies that were formed by fluid-present melting, nor migmatites that were formed through biotite dehydration melting. However

leucogranites recording geochemical signatures fluid-present melting have been reported elsewhere in the Himalaya, particularly east of the Everest region and in SE Tibet (e.g. Gao et al., 2017; Gao et al., 2024).

Conclusions

Migmatite and leucogranite samples outcropping near Badrinath, Garhwal Himalaya, India, document petrographic and mineral chemistry indicators of three different melting reactions. Migmatite samples containing sillimanite, plagioclase and little (or no) K-feldspar in the leucosome (Group 1) preserve a record of melting in the presence of free fluids. K-feldspar, plagioclase, muscovite and biotite in these samples contain higher concentrations of Ba and Eu, and lower Rb/Sr (the latter most notably in K-feldspar, muscovite and biotite). Muscovite and biotite in these samples furthermore generally contain lower concentrations of Sn. These samples yield Ti in biotite temperatures of <750°C.

Migmatite and leucogranite samples that contain porphyroblastic or phenocrystic K-feldspar with perthitic albite lamellae and inclusions of irregular quartz and embayed plagioclase, lenticular clusters of K-feldspar and/or topotactic replacement of plagioclase and greatly reduced plagioclase abundance (Group 2), preserve a record of muscovite dehydration melting. K-feldspar, plagioclase, muscovite and biotite in these samples contain lower concentrations of Ba and Eu, and higher Rb/Sr (the latter most obviously in K-feldspar, muscovite and biotite). Muscovite and biotite in these samples furthermore generally contain variable concentrations of Sn. These samples yield Ti in biotite temperatures of >750°C.

A leucogranite sample containing garnet with high concentrations of randomly-oriented rutile micro-inclusions (Group 3), preserves (rare) evidence for biotite dehydration melting. K-feldspar, plagioclase and muscovite in this sample contain the lowest Ba concentrations and highest Rb/Sr (the latter most obviously in K-feldspar and muscovite). This sample contained no biotite but exsolution of acicular rutile across garnet core-mantle boundaries suggests peritectic core formation at temperatures >800°C.

The chemical signatures and trends in the major phases across these samples mirror those previously recorded in bulk rock signatures and confirm the role of the relative contributions of these phases in controlling the bulk chemistry during melting. The compositional variability of the

constituent minerals may reflect local bulk composition control or may indicate the progression of different melt reactions; this was unresolvable in our dataset.

The migmatite and leucogranite occurrences from the Garwhal Himalaya region reveal intriguing evidence of distinct melting reactions despite sharing similar thermal histories. These rocks predominately record either melting in the presence of free fluids or muscovite dehydration melting, but never both. This suggests that rocks which experienced fluid-present melting cease to react once the muscovite has been consumed, showcasing the complex interplay between mineral compositions and melting processes.

Acknowledgments

CO acknowledges financial assistance from a Natural Environment Research Council postgraduate studentship awarded through the CENTA doctoral training partnership. He gratefully extends thanks to Kay Knight and Michelle Higgins for their sterling work making all the thin sections and Aditya Kharya for assistance in the field.

Samples were collected in the Garhwal Himalaya, Uttarakhand, India in October 2018, under permit from the Wadia Institute of Himalayan Geology, an autonomous institution of the Department of Science & Technology, Government of India.

References

Ashley, K. T. and Law, R. D. (2015) ‘Modeling prograde TiO2 activity and its significance for Ti-in-quartz thermobarometry of pelitic metamorphic rocks’, *Contributions to Mineralogy and Petrology*, vol. 169, no. 2, p. 23 [Online]. DOI: 10.1007/s00410-015-1118-7.

Axler, J. A. and Ague, J. J. (2015) ‘Oriented multiphase needles in garnet from ultrahigh-temperature granulites, Connecticut, U.S.A.’, *American Mineralogist*, vol. 100, no. 10, pp. 2254–2271 [Online]. DOI: 10.2138/am-2015-5018.

Borisov, A. and Aranovich, L. (2020) ‘Rutile solubility and TiO2 activity in silicate melts: An experimental study’, *Chemical Geology*, vol. 556, p. 119817 [Online]. DOI: 10.1016/j.chemgeo.2020.119817.

Breton, N. L. and Thompson, A. B. (1988) 'Fluid-absent (dehydration) melting of biotite in metapelites in the early stages of crustal anatexis', *Contributions to Mineralogy and Petrology*, vol. 99, no. 2, pp. 226–237 [Online]. DOI: 10.1007/BF00371463.

Brown, M. (2007) 'Crustal melting and melt extraction, ascent and emplacement in orogens: mechanisms and consequences', *Journal of the Geological Society*, vol. 164, no. 4, pp. 709–730 [Online]. DOI: 10.1144/0016-76492006-171.

Brown, M. (2013) 'Granite: From genesis to emplacement', *GSA Bulletin*, vol. 125, no. 7–8, pp. 1079–1113 [Online]. DOI: 10.1130/B30877.1.

Chambers, J. A. and Kohn, M. J. (2012) 'Titanium in muscovite, biotite, and hornblende: Modeling, thermometry, and rutile activities of metapelites and amphibolites', *American Mineralogist*, vol. 97, no. 4, pp. 543–555 [Online]. DOI: 10.2138/am.2012.3890.

Clemens, J.D. and Vielzeuf, D., 1987. Constraints on melting and magma production in the crust. *Earth and Planetary Science Letters*, *86*(2-4), pp.287-306.

Deer, W. A., Howie, R. A. and Zussman, J. (2013) 'An Introduction to the Rock-Forming Minerals', [Online]. DOI: 10.1180/DHZ (Accessed 26 October 2022).

Dorais, M. J. and Campbell, S. (2022) 'Peritectic and phenocrystic garnet accumulation and the origin of strongly peraluminous granitic rocks: The Flagstaff Lake Igneous Complex, Maine', *Lithos*, vol. 418–419, p. 106680 [Online]. DOI: 10.1016/j.lithos.2022.106680.

Dorais, M. J. and Spencer, C. J. (2014) 'Revisiting the importance of residual source material (restite) in granite petrogenesis: The Cardigan Pluton, New Hampshire', *Lithos*, vol. 202–203, pp. 237–249 [Online]. DOI: 10.1016/j.lithos.2014.05.007.

Dyck, B., Waters, D. J., St-Onge, M. R. and Searle, M. P. (2020) 'Muscovite dehydration melting: Reaction mechanisms, microstructures, and implications for anatexis', *Journal of Metamorphic Geology*, vol. 38, no. 1, pp. 29–52 [Online]. DOI: 10.1111/jmg.12511.

Erdmann, S., Scaillet, B. and Kellett, D. A. (2012) 'Textures of Peritectic Crystals as Guides to Reactive Minerals in Magmatic Systems: New Insights from Melting Experiments', *Journal of Petrology*, vol. 53, no. 11, pp. 2231–2258 [Online]. DOI: 10.1093/petrology/egs048.

Gao, L.-E., Zeng, L. and Asimow, P. D. (2017) 'Contrasting geochemical signatures of fluid-absent versus fluid-fluxed melting of muscovite in metasedimentary sources: The Himalayan leucogranites', *Geology*, vol. 45, no. 1, pp. 39–42 [Online]. DOI: 10.1130/G38336.1.

Gao, L.E., Zeng, L., Zhao, L., Yan, L., Hou, K. and Wang, Q., 2024. Fluid-fluxed melting in the Himalayan orogenic belt: Implications for the initiation of EW extension in southern Tibet. *Bulletin*, *136*(3-4), pp.989-1002.

Gardien, V., Thompson, A., Grujic, D. and Ulmer, P. (1995) 'Experimental melting of biotite + plagioclase + quartz ± muscovite assemblages and implications for crustal melting', *Journal of Geophysical Research*, vol. 100, p. 15581 [Online]. DOI: 10.1029/95JB00916.

Harris, N., Massey, J. and Inger, S. (1993) 'The role of fluids in the formation of High Himalayan leucogranites', *Geological Society, London, Special Publications*, The Geological Society of London, vol. 74, no. 1, pp. 391–400 [Online]. DOI: 10.1144/GSL.SP.1993.074.01.26.

Harris, N., Ayres, M. and Massey, J. (1995) 'Geochemistry of granitic melts produced during the incongruent melting of muscovite: Implications for the extraction of Himalayan leucogranite magmas', *Journal of Geophysical Research: Solid Earth*, vol. 100, no. B8, pp. 15767–15777 [Online]. DOI: 10.1029/94JB02623.

Henry, D. and Guidotti, C. (2002) 'Titanium in biotite from metapelitic rocks: Temperature effects, crystal-chemical controls, and petrologic applications', *American Mineralogist*, vol. 87, pp. 375–382 [Online]. DOI: 10.2138/am-2002-0401.

Hwang, S. L., Yui, T. F., Chu, H. T., Shen, P., Schertl, H. P., Zhang, R. Y. and Liou, J. G. (2007) 'On the origin of oriented rutile needles in garnet from UHP eclogites', *Journal of Metamorphic Geology*, vol. 25, no. 3, pp. 349–362 [Online]. DOI: 10.1111/j.1525-1314.2007.00699.x.

Hwang, S.-L., Shen, P., Chu, H.-T. and Yui, T.-F. (2016) 'On the forbidden and the optimum crystallographic variant of rutile in garnet', *Journal of Applied Crystallography*, International Union of Crystallography, vol. 49, no. 6, pp. 1922–1940 [Online]. DOI: 10.1107/S1600576716014151.

Inger, S. and Harris, N. B. W. (1992) 'Tectonothermal evolution of the High Himalayan Crystalline Sequence, Langtang Valley, northern Nepal', *Journal of Metamorphic Geology*, vol. 10, no. 3, pp. 439–452 [Online]. DOI: 10.1111/j.1525-1314.1992.tb00095.x.

Inger, S. and Harris, N. (1993) 'Geochemical Constraints on Leucogranite Magmatism in the Langtang Valley, Nepal Himalaya', *Journal of Petrology*, vol. 34, no. 2, pp. 345–368 [Online]. DOI: 10.1093/petrology/34.2.345.

Jain, A., M., S., Seth, P., Kanyan, L., Carosi, R., Montomoli, C., Iaccarino, S. and Mukherjee, P. k (2014) 'The Higher Himalayan Crystallines, Alaknanda – Dhauli Gan-ga Valleys, Garhwal Himalaya, India', *Journal of the Virtual Explorer*, vol. 47, p. 35.

Jenner, F. E. and O'Neill, H. S. C. (2012) 'Major and trace analysis of basaltic glasses by laser-ablation ICP-MS', *Geochemistry Geophysics Geosystems*, vol. 13, no. 3 [Online]. Available at https://oro.open.ac.uk/38166/ (Accessed 18 October 2022).

Ji, M., Gao, X.Y. and Zheng, Y.F., 2023. The petrogenetic relationship between migmatite and granite in the Himalayan orogen: Petrological and geochemical constraints. *Lithos*, *444*, p.107110.

Jung, S., Pfänder, J.A., Mezger, K., Hellebrand, E. and Brandt, S., 2022. Polyphase growth history of peritectic garnet from a granite: Trace-element zonation, Lu-Hf ages and their significance for the duration of granite-forming processes. *Lithos*, *418*, p.106675. DOI: 10.1016/j.lithos.2022.106675.

Kohn, M. J. and Spear, F. (2000) 'Retrograde net transfer reaction insurance for pressure-temperature estimates', *Geology*, vol. 28, no. 12, pp. 1127–1130 [Online]. DOI: 10.1130/0091-7613(2000)28<1127:RNTRIF>2.0.CO;2.

Kunz, B.E., Warren, C.J., Jenner, F.E., Harris, N.B. and Argles, T.W., 2022. Critical metal enrichment in crustal melts: The role of metamorphic mica. *Geology*, *50*(11), pp.1219-1223.

Müller, A., Kearsley, A., Spratt, J., Seltmann. R., (2012) Petrogenetic implications of magmatic garnet in granitic pegmatites from Southern Norway. *The Canadian Mineralogist* 50 (4): 1095–1115.

Patiño-Douce, A.E., Humphreys, E.D. and Johnston, A.D., 1990. Anatexis and metamorphism in tectonically thickened continental crust exemplified by the Sevier hinterland, western North America. *Earth and Planetary Science Letters*, *97*(3), pp.290-315.

Patiño Douce, A.E. and Harris, N., 1998. Experimental constraints on Himalayan anatexis. *Journal of petrology*, *39*(4), pp.689-710.

Paton, C., Hellstrom, J., Paul, B., Woodhead, J. and Hergt, J., 2011. Iolite: Freeware for the visualisation and processing of mass spectrometric data. *Journal of Analytical Atomic Spectrometry*, *26*(12), pp.2508-2518.

Paul, S. K. (1998) 'Geology and tectonics of the Central Crystallines of northeastern Kumaun Himalaya, India', *Journal of Nepal Geological Society*, vol. 18, pp. 151–167 [Online]. DOI: 10.3126/jngs.v18i0.32249.

Phillips, S.E., Argles, T.W., Warren, C.J., Harris, N.B. and Kunz, B.E., 2023. Kyanite petrogenesis in migmatites: resolving melting and metamorphic signatures. *Contributions to Mineralogy and Petrology*, *178*(2), p.10.

Pickering, J. M. and Johnston, D. A. (1998) 'Fluid-Absent Melting Behavior of a Two-Mica Metapelite: Experimental Constraints on the Origin of Black Hills Granite', *Journal of Petrology*, vol. 39, no. 10, pp. 1787–1804 [Online]. DOI: 10.1093/petroj/39.10.1787.

Proyer, A., Habler, G., Abart, R., Wirth, R., Krenn, K. and Hoinkes, G. (2013) 'TiO2 exsolution from garnet by open-system precipitation: evidence from crystallographic and shape preferred orientation of rutile inclusions', *Contributions to Mineralogy and Petrology*, vol. 166, no. 1, pp. 211–234 [Online]. DOI: 10.1007/s00410-013-0872-7.

Rosenberg, C. L. and Handy, M. R. (2005) 'Experimental deformation of partially melted granite revisited: implications for the continental crust', *Journal of Metamorphic Geology*, vol. 23, no. 1, pp. 19–28 [Online]. DOI: 10.1111/j.1525-1314.2005.00555.x.

Schiller, D. and Finger, F. (2019) 'Application of Ti-in-zircon thermometry to granite studies: problems and possible solutions', *Contributions to Mineralogy and Petrology*, vol. 174, no. 6, p. 51 [Online]. DOI: 10.1007/s00410-019-1585-3.

Spencer, C. J., Harris, R. A. and Dorais, M. J. (2012a) 'The metamorphism and exhumation of the Himalayan metamorphic core, eastern Garhwal region, India', *Tectonics*, vol. 31, no. 1 [Online]. DOI: 10.1029/2010TC002853 (Accessed 12 July 2022).

Spencer, C. J., Harris, R. A. and Dorais, M. J. (2012b) 'Depositional provenance of the Himalayan metamorphic core of Garhwal region, India: Constrained by U–Pb and Hf isotopes in zircons', *Gondwana Research*, vol. 22, no. 1, pp. 26–35 [Online]. DOI: 10.1016/j.gr.2011.10.004.

Taylor, J. and Stevens, G. (2010) 'Selective entrainment of peritectic garnet into S-type granitic magmas: Evidence from Archaean mid-crustal anatectites', *Lithos*, vol. 120, no. 3, pp. 277–292 [Online]. DOI: 10.1016/j.lithos.2010.08.015.

Valdiya, K. S. (1979), An outline of the structtural set-up of the Kumaun Himalaya, J. Geol. Soc. India, 20, 145–157.

Vigneresse, J. L., Barbey, P. and Cuney, M. (1996) 'Rheological Transitions During Partial Melting and Crystallization with Application to Felsic Magma Segregation and Transfer', *Journal of Petrology*, vol. 37, no. 6, pp. 1579–1600 [Online]. DOI: 10.1093/petrology/37.6.1579.

Weinberg, R. F. and Hasalová, P. (2015) 'Water-fluxed melting of the continental crust: A review', *Lithos*, vol. 212–215, pp. 158–188 [Online]. DOI: 10.1016/j.lithos.2014.08.021.

Wu, C.-M. and Chen, H. (2015) 'Revised Ti-in-biotite geothermometer for ilmenite- or rutile-bearing crustal metapelites', *Science Bulletin*, vol. 60 [Online]. DOI: 10.1007/s11434-014-0674-y.

Figure Captions

Figure 1: P-T diagram showing the the melt-forming reactions in metapelitic systems (after Weinberg & Haslova, 2015)

Figure 2: Map showing sample localities. (a) Simplified geological map of the GHS in the eastern Garhwal, showing the Alaknanda and Dhauliganga valleys, after Spencer et al., 2012a and references therein. Box shows location of (b). Inset shows the study area in relation to India. (b) Map of sampling localities along the Alaknanda and Rishi Ganga valleys, around Badrinath in the Garhwal Himalaya. Coordinates are in WGS84. Locality 11 is 15.5 km south-southeast of Hanuman Chatti, near Joshimath

Figure 3: Composite images showing Group 1 and 2 sample field relations and petrography. (a) Thin section photomicrograph of Group 1 migmatite 08. (b) False colour SEM image of diatexitic Group 1 migmatite 07c. The leucosomes are the irregular areas of coarser Qz and Pl (centre and lower left). (c) Thin section photomicrograph of Group 2 migmatite 4b. (d) False colour SEM image of sample Group 2 migmatite 7a. The Kfsp defines the larger patches of leucosome, commonly also rimmed by Mus-Sil and Bt. (e) BSE image of sample 4a showing perthitic K-feldspar phenocrysts and K-feldspar overgrowing plagioclase. (f) Photomicrograph of sample 4a showing plagioclase with K-feldspar overgrowth/replacement in the mesosome

Figure 4: (a) Garnet in sample 1d showing lobate quartz inclusion (Group 2). (b, c) Garnet in sample 6 (Group 3), showing clear core rim distinction. (c) At the boundary of the core and rim fine needles or rutile can be observed

Figure 5: Violin plots of calculated Ti in Bt temperatures for Group 1 (green) and Group 2 (blue) migmatite (02a, 04a, 04b, 07a, f02) and leucogranite (01d, 03, 07b, f04) samples. All data are from EDS apart from samples f02 and f04, for which the LA-ICP-MS data are plotted. The dashes mark the upper quartile, median and lower quartile respectively. The width of the "violins" corresponds to the number of datapoints yielding that value of temperature

Figure 6: Field photograph of cross-cutting relationships in Locality 7. Inset shows interpretation of cross-cutting leucosome relationships with the yellow leucogranite (sample 7b) cross-cutting the blue leucosome (not sampled). Migmatite samples 7a and 7c showed different leucosome expressions and proportions

Figure 7: Rb/Sr in K-feldspar plotted against (a) Ba and (b) Eu

Figure 8: Rb/Sr in plagioclase plotted against (a) Ba and (b) Eu

Figure 9: Rb/Sr in muscovite plotted against (a) Ba and (b) Sn

Figure 10: Rb/Sr in biotite plotted against (a) Ba and (b) Sn

Figure 11: Garnet composition data. (a) Major element profile of garnet in Group 2 migmatite f02. (b) Major element profile of garnet in Group 2 leucogranite 1d. (c) Major element profile of garnet in Group 3 leucogranite 6

Table Captions

Table 1: Summary of sample groups

Table 2: Calculated Ti in Bt temperatures, presented to the nearest 1°C. L=leucogranite, M=migmatite, n= number of datapoints lying within the Wu and Chen calibration range.

This manuscript has been submitted for peer review in Contributions to Mineralogy and Petrology. Subsequent versions of this manuscript may have slightly different content. If accepted, the final version will be available via the Peer-reviewed DOI link on the EarthArxiv website. The authors welcome questions about this work.

Online Datasets

Datasets relating to this submission are available on the Open University Open Data repository. They are not formatted in the same way as the peer-reviewed Supplementary Data but provide all the underpinning datasets.

https://ordo.open.ac.uk/authors/Charlie_Oldman/16473492